

## Chapter 4: Steering and Orbit Correction

### 4.1 Motivation

Precise control of centroid orbit is necessary for good beam recirculation, with low losses due to large centroid deviations. This allows for observation of beam losses due to more complex effects, such as resonant excitation of particle and/or beam envelope amplitudes, as well as longitudinal losses. The proposed quasi-integrable nonlinear optics experiment has, as its lowest-order, most straightforward diagnostic, a characterization of resonantly driven beam losses with and without nonlinear damping. Therefore, a reduction of transverse scraping losses is imperative for observation of these likely slower loss rates. Additionally, the nonlinear optics experiments require a low-current, high-emittance  $60\mu A$  beam. A large emittance beam corresponds to a large cross-section beam in configuration space, which places a more stringent requirement on steering tolerances.

In an ideal linear accelerator, there exists a "reference trajectory," which describes the path of an ideal particle. This trajectory is typically centered within the focusing quadrupoles and the beam pipe. A beam with imperfect injection conditions will oscillate about the ideal trajectory. In this section, we define "first-turn orbit" to mean the measured or simulated centroid trajectory on the first

turn. "Closed orbit" refers to the orbit about which the trajectory oscillates. This is also referred to as the "equilibrium orbit." Ideally this orbit is centered in the quadrupoles, but due to background field, alignment errors and number of available correctors, it is only possible to minimize orbit deviation from quadrupole centers.

In general, for straightforward operation of UMER, lowest-possible deviation of beam centroid from quadrupole centers in multi-turn operation is desirable, for the smallest coupling between focusing strength and closed orbit deviation. As seen in Section ??, the dynamic aperture of the quasi-integrable octupole lattice suffers greatly for orbit distortions, and it is desirable to minimize centroid offset from octupole centers in the octupole insert.

## 4.2 *Considerations for low-rigidity electron beam*

In typical high-energy accelerating or storage rings (for which steering algorithms are well-developed), the beam travels in straight lines between steering elements (dipoles or off-centered quadrupoles), effectively tracing out an N-sided polygon where N is the number of dipoles. Steering in UMER is complicated by the fact that at low-energies, the beam is significantly bent by background, ambient fields. For a 10 keV electron beam, rigidity  $B\rho = \frac{p}{q}$  is 338.859 G-cm. The required integrated field to bend the beam  $10^\circ$  is 59.154 G-cm. Given an average ambient vertical field of  $\approx 400$  mG, per 32 cm cell, the integrated field is  $32 * 0.400 = 12.8$  G-cm. Therefore, approximately 22% of the total horizontal bending in the ring is due to the ambient vertical fields. The ambient horizontal field is weaker, on

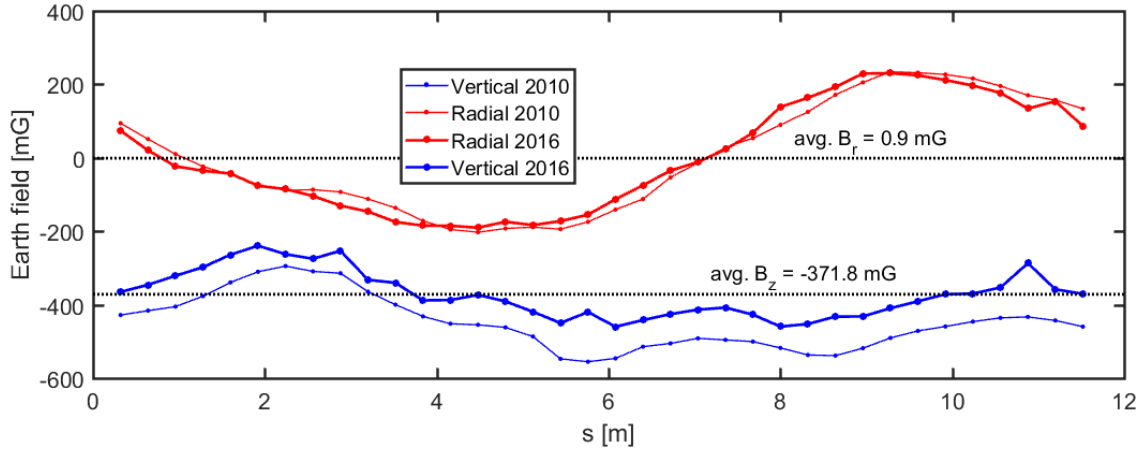


Fig. 4.1: Ambient fields measured at UMER dipoles, from Dave Sutter measurements 6/1/2010 and 7/22/2016.

average  $< 1$  mG, which gives only a small orbit distortion (requiring only a small correction) from turn-to-turn. However, local closed orbit distortions due to the horizontal fields can be large (up to  $\approx 200$  mG), and large vertical corrections are necessary to minimize deviation from quadrupole centers. Measured ambient field data can be seen in Figs. 4.1 and 4.2.

Because the beam is immersed in a bending field, in the perfectly aligned case a beam orbit that is centered in the quadrupoles is required to be displaced in the BPMs, as in Fig. 4.3. Simple calculations with a constant background field show that we expect the ideal orbit to be radially displaced by [todo:]. However, in the case of azimuthally-varying ambient fields and displacements up to several millimeters, we expect larger displacements of the "best-possible" orbit.

Steering in the ring is controlled by 36 horizontal bending dipoles, which determine the shape of the horizontal closed orbit, and which can be independently

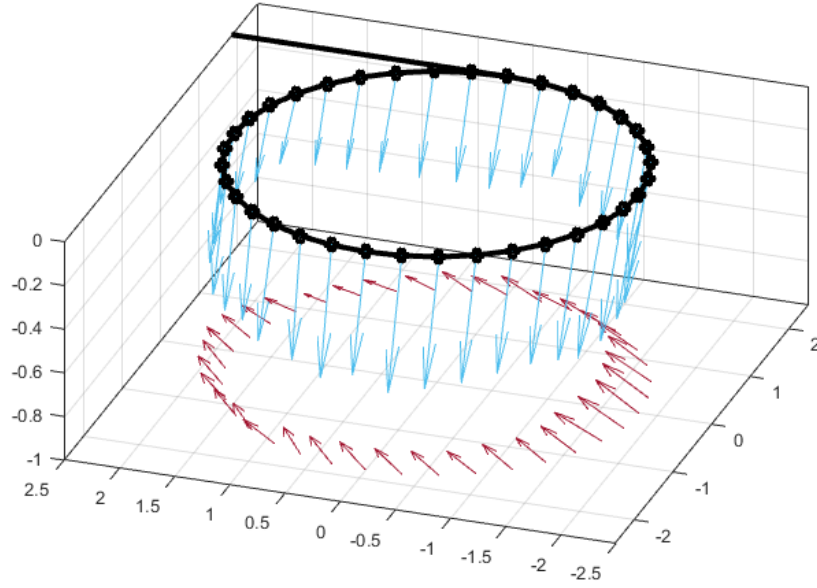


Fig. 4.2: Ambient field data vectors, including xy projection. x,y units are meters, z-axis is milli-Gauss.

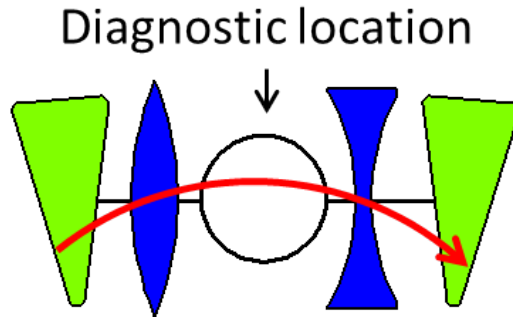


Fig. 4.3: Diagram of beam position in diagnostic (BPM) for an orbit that is horizontally centered in the quadrupoles.

adjusted to optimize the orbit. This is different from the typical case of a larger ring, which uses fixed dipoles and adjustable corrector magnets. There is 1 independent horizontal dipole every 2 quadrupoles. Vertical correction is made with 18 printed circuit corrector magnets located at pipe flanges, which are named "RSV" magnets. There is 1 RSV corrector every 4 quadrupoles. Additional vertical correctors have been added and proposed, as described in Section ???. Steering near injection is controlled by 6 vertical and horizontal corrector magnets in the injection line, in the "SDH" and "SDV" families. Additionally, there are two correctors (one horizontal and one vertical) in the ring near the intersection of the injection pipe (the "Y-section"), named "SDR6H" and "SDR6V."

### 4.3 UMER Steering Magnets

Tab. 4.1: UMER Steering magnet strengths

Magnet Name	length [cm]	radius [cm]	Integ. Field / A [G-cm/A]	strength [ $^{\circ}$ /A]
BD	4.44	2.87	19.917	3.37
PD	4.40	4.40	1.913	0.32
RSV	3.80	5.75	3.886	0.66
SD	2.37	4.73	3.317	0.56
SSV	1.54	2.79	3.627	0.61

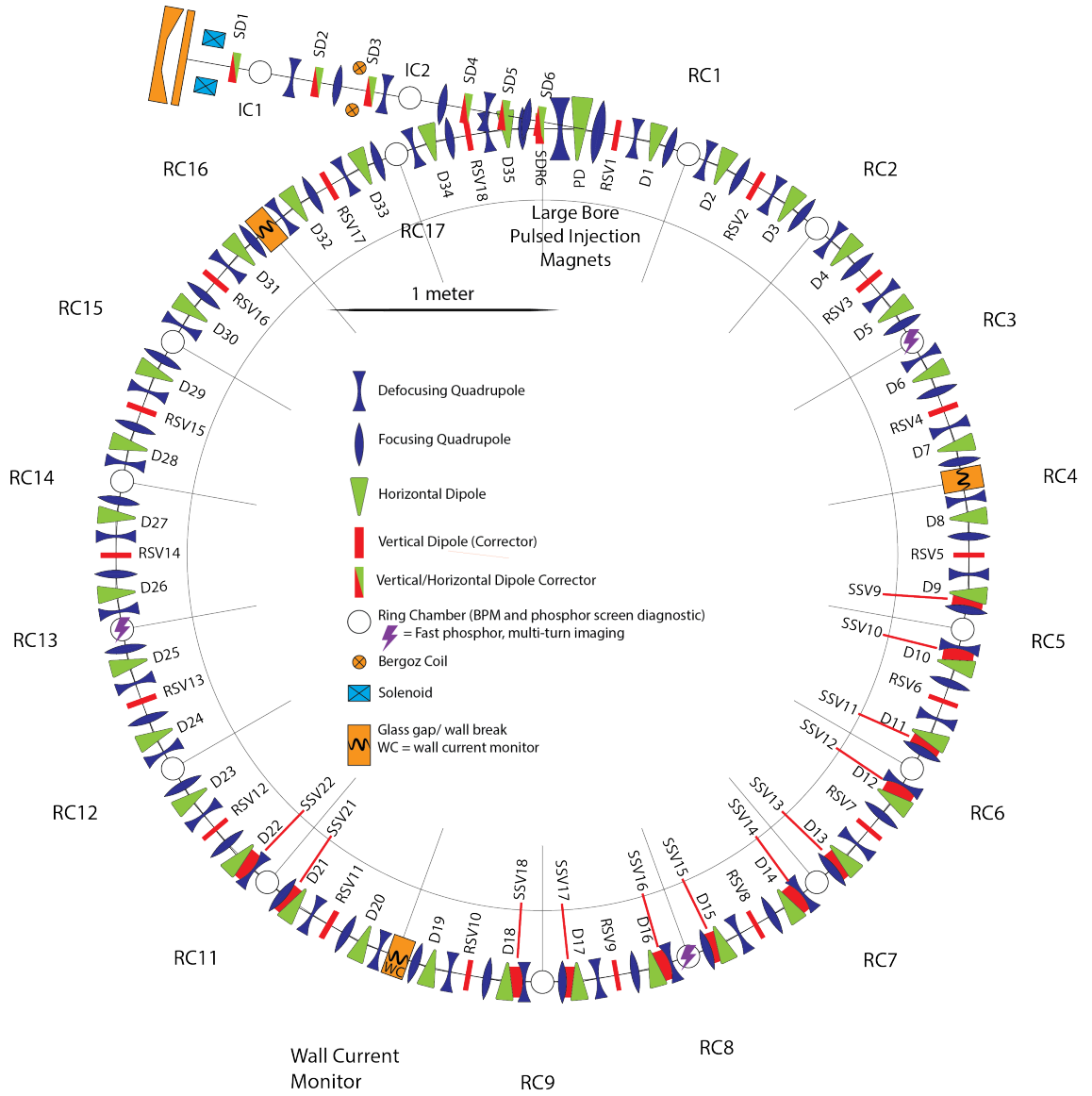


Fig. 4.4: UMER Diagram with all steerers labelled. SSV family is discussed in Section 4.8

## 4.4 Prior Approach

An alternative approach to steering was developed using a steering procedure with local corrections to ensure the equilibrium orbit is centered (or as close to centered as possible) in the quadrupoles. This is unique from the response matrix method, in which a global correction is calculated that aims to center the equilibrium orbit at the 14 BPM locations. The steering algorithm is a methodical, "front to back" approach that first minimizes the position of the beam in the quadrupoles on the first turn then minimizes orbit deviations in subsequent turns. This algorithm should result in smaller local orbit excursions from quadrupole centers, since it utilizes 36 position data points at quadrupole locations for the first turn orbit as opposed to 14 at the BPMs. This is proposed as a alternative to the response matrix steering algorithm [1], and may be more useful for applications where orbit centering in the quadrupoles is essential.

The remainder of this chapter describes the tools and algorithmic approach to centering the first turn orbit in the quadrupole centers. First I describe the quad-as-BPM procedure for measuring first-turn centroid position at the quadrupoles (Section 4.5). Then I summarize the application of various algorithms to set horizontal and vertical steerers in Section ??, including theoretical "best-case" orbit excursions and proposed vertical steering upgrades to meet the dynamic aperture requirements for the nonlinear optics experiments. This includes first-turn data taken during ring steering tests. Section 4.7 lays out a sample steering procedure, including injection and multi-turn optimization routines.

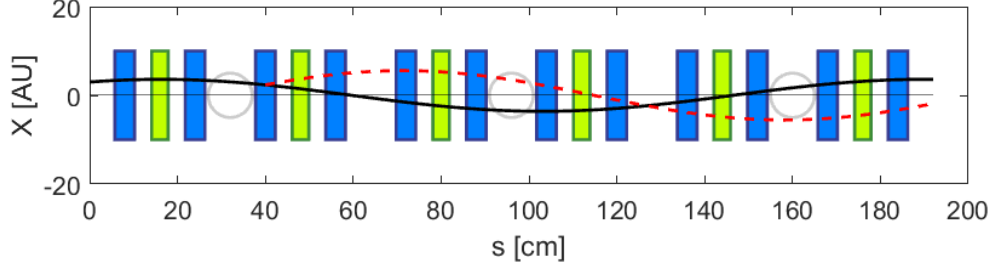


Fig. 4.5: Diagram of UMER beamline, with quadrupoles (blue), dipoles (green) and BPMs (circles). Black curve is possible centroid trajectory, dashed-red curve is perturbed centroid due to change in quadrupole strength at 40 cm. Phase advance per cell (32 cm) is  $66.4^\circ$ .

#### 4.5 Quadrupole as BPM technique

First-turn position data is extrapolated from quadrupole response data, also called "quad as BPM" or "virtual BPM." A beam that is off-centered in a quadrupole will experience a dipole force acting on the centroid motion as well as a quadrupole focusing force that acts on the beam envelope, as shown in Fig. 4.5. The strength of the dipole kick will depend on the position of the centroid in the quadrupole as well as strength of the quadrupole. Variation of the quadrupole strength will cause variation of the centroid as detected on a downstream BPM. Knowledge of the centroid transformation between quadrupole and BPM allows reconstruction of the beam position.

In a lattice with low phase advance per cell (such as UMER, with  $66.4^\circ$  and  $67.5^\circ$  in the x,y planes), the particle motion is approximately sinusoidal, described by:



$$x(s) = A_1 \cos \frac{\sigma}{L}s + A_2 \sin \frac{\sigma}{L}s \quad (4.1)$$

The derivative of this motion is

$$x'(s) = \frac{dX}{ds} = -A_1 \frac{\sigma}{L} \sin \frac{\sigma}{L}s + A_2 \frac{\sigma}{L} \cos \frac{\sigma}{L}s \quad (4.2)$$

Generally, the centroid is not confined to the reference orbit (the orbit that goes through the center of every quad), so the equilibrium centroid orbit oscillates with a frequency of  $2\pi \times \nu$ , with amplitudes  $A$ . Now, let's consider an orbit that has been perturbed, due to changing the strength of a single quad. We treat the quadrupole as "thin," an appropriate simplification when phase advance is low. Using the analog of thin lens optics in the paraxial approximation,  $\Delta x' \approx \tan \Delta x' = \frac{x_Q}{f}$  where  $x_Q$  is the centroid offset in the quad and  $f$  is the focal length. For a thin quadrupole,  $\frac{1}{f} = \frac{G}{B\rho}$  for integrated gradient  $G$  and magnetic rigidity  $B\rho$ . For UMER ring quadrupoles,  $G = 13.50I$  [Gauss/A] and for 10 keV electrons,  $B\rho = 338.85$  G-cm.

Consider a perturbed orbit  $\tilde{x}(s) = x(s) + \delta x(s)$ , where  $s = 0$  is the perturbed quad location. The initial conditions are  $\tilde{x}(0) = x(0)$  and  $\tilde{x}'(0) = x'(0) + \Delta x'_Q$  where  $\Delta x'_Q = x(\frac{G\Delta I}{B\rho})$  is the change in angle due to perturbation on the quad. Letting  $\delta x(s) = B_1 \cos \sigma s/L + B_2 \sin \sigma s/L$  and applying these initial conditions, we find  $B_1 = 0$ ,  $B_2 = x_Q L/\sigma \times G\Delta I/B\rho$  and the perturbed orbit is:

$$\tilde{x}(s) = x(s) + x_Q \frac{L G \Delta I}{\sigma B \rho} \sin \frac{\sigma}{L}s \quad (4.3)$$

With variation of the quadrupole strength, we find the dependence of the

centroid position in a downstream BPM is linear in the position in the quadrupole,  $x_Q$ :

$$\frac{d\tilde{x}(s_{BPM})}{d\Delta I} = x_Q \frac{L}{\sigma} \frac{G}{B\rho} \sin \frac{\sigma}{L} s_{BPM} \quad (4.4)$$

In the approach described here, we recover the first-turn position in the quadrupoles by measuring the slope  $\frac{d\tilde{x}(s_{BPM})}{d\Delta I}$ . A model of the ring using the VRUMER beam tracking code is used to calculate the constant  $\frac{L}{\sigma} \frac{G}{B\rho} \sin \frac{\sigma}{L} s_{BPM}$ , the result is a measurement of  $x_Q$ . This is an essentially identical method to that described by Kamal Poor Rezaei [2], with the main difference being the use of the VRUMER beam tracking code to calibrate position, rather than a transfer matrix calculation.

VRUMER, described in detail in Appendix [TBD], is a simple orbit integrator written in Matlab, originally developed by Irving Haber to model transverse beam centroid behavior and test UMER-specific steering algorithms. The model used here includes the measured background earth field, applied as a continuously acting, lab-frame-position dependent force based on linear interpolation between measurement points at the 36 dipoles. This model does not include centroid kicks as a result of magnet fringe fields or the steering effect of the offset YQ magnet, although the framework can support these refinements.

At an operating point of 1.826 A, the UMER 6 mA beam has  $\nu_x = 6.636$ ,  $\nu_y = 6.752$  [3]. This corresponds to betatron wavelengths  $\lambda_x = 1.736$  m,  $\lambda_y = 1.706$  m. In the VRUMER simulation, horizontal and vertical tunes are equal (no edge focusing),  $\nu = 6.293$ , equivalently  $\lambda = 1.83$  m. In this case, quadrupole strength

parameters were set according to standard hard-edged approximation for the UMER quadrupoles: length= 4.475 cm, peak strength  $g = 3.609$  G/cm, hard-edge factor  $f = 0.8354$ .

#### 4.5.1 Systematic Error in Quad-as-BPM Calibration

The previous section begs the question, what is the amount of systematic error introduced by differences between reality and the model used for calibration (in this case, VRUMER). Most notably, bare tune in the model and measured tune differ by  $\Delta\nu_x = 0.340$  horizontally,  $\Delta\nu_y = 0.459$  vertically. It is convenient to define phase advance per cell,  $\sigma = \frac{2\pi\nu}{36}$ . Additionally, there are measurement errors included in the measurement of position with BPM.

Examining the formula for  $x_Q$  from Eq. 4.4 above, re-written here as:

$$x_Q = \frac{\sigma}{L} \frac{d\tilde{x}_{BPM}}{d\Delta I} \sin^{-1} \frac{\sigma}{L} s_{BPM} \quad (4.5)$$

Applying error analysis and assuming no significant error is introduced by our choice of  $L$ ,  $G$ ,  $B\rho$ , or  $s_{BPM}$  in the model, we find the position error to be dependent on errors in the measured slope  $m$ ,  $\sigma_m$ , and the systematic error of the model phase advance  $\sigma$ ,  $\sigma_\sigma$ .

$$\frac{\sigma_{x_Q}}{x_Q} = \left[ 1 - \frac{s_{BPM}}{L} \cot \frac{\sigma}{L} s_{BPM} \right] \frac{\sigma_\sigma}{\sigma} + \frac{\sigma_m}{m} \quad (4.6)$$

In this case, error  $\sigma_m$  encompasses to statistical and systematic noise, as well as systematic calibration errors, related to the collection and processing of BPM data.

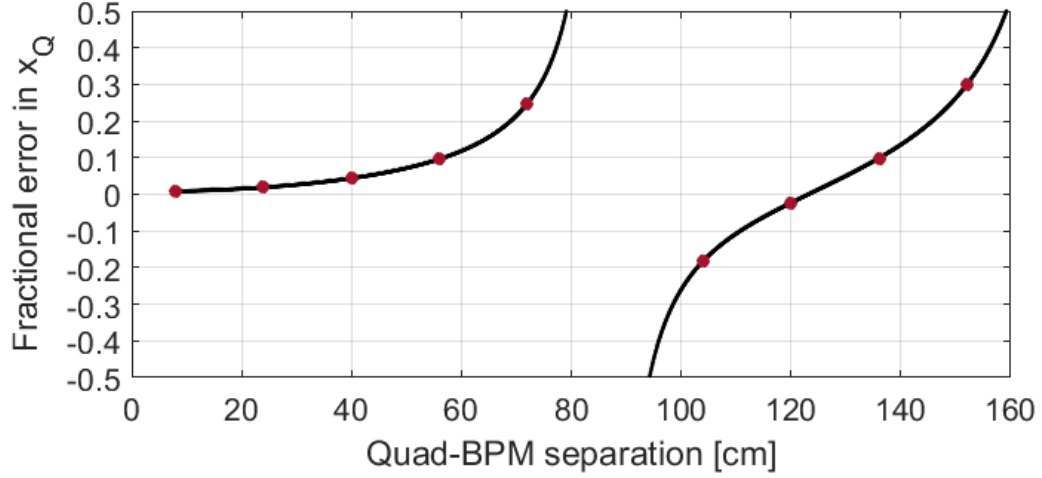


Fig. 4.6: Fractional error in quad-as-BPM position due to phase error, versus quad and BPM separation

For all the data shown here,  $\sigma_m$  was taken to be the 90% confidence bounds of the slope for the linear fit to the measured BPM position versus quadrupole strength curve. This encompasses shot-to-shot noise and nonlinearities introduced by beam scraping. Additionally, background was subtracted from scope traces to reduce the effect of systematic, repeatable noise picked up by the BPM amplifiers.

$\sigma_\sigma$  is an error introduced by using the VRUMER model to calibrate quadrupole response data, and can be reduced by tweaking the focusing strength in the model.

Fig. 4.6 shows the dependence of the fractional error of measured position in the quadrupole,  $x_Q$ , as a function of separation between quadrupole and BPM used to measure quadrupole response. In this case,  $\sigma_\sigma$  is taken to be the systematic error in phase advance between the VRUMER model and UMER experiment,  $\sigma_\sigma = |\sigma_{sim} - \sigma_{exp}| = 0.06$ . Only 8 discrete quad-BPM separations exist, in the range [8, 24, 40, ...120] cm.

Tab. 4.2: "Next-downstream" Quad-BPM pairs with separations near half of a betatron wavelength, which results in large errors in the quad-as-BPM method.

Quad #	Nearest BPM
QR14	RC5
QR38	RC11
QR62	RC17
QR70	RC1 (turn 2)

As seen from Eq. 4.6, the error approaches  $\infty$  where  $\frac{\sigma}{L}s_{BPM} = n\pi$ . This is the point where the betatron wavelength is equal to the quad-BPM separation, a null point of the perturbed orbit  $\delta x(s) = x_Q \frac{L}{\sigma} \frac{G\Delta I}{B\rho} \sin \frac{\sigma}{L}s$ . Near this null, the returned quad-as-BPM measurement will have large errors, and in general be very sensitive to error in the BPM measurement as well as differences in the model and experiment.

In standard UMER operation, the BPM spacing is 64 cm (see Fig. 4.5), and the associated error is maximum 10%. However, 4 BPM's are omitted for injection, longitudinal focusing and the wall current monitor. Larger errors are permitted at larger separations. Table 4.2) shows quadrupole-BPM pairs with fractional error  $> 1$ . The spacing for these 4 pairs is 88 cm, close to half the betatron wavelength,  $\frac{\lambda}{2} \approx 86cm$ .

In subsequent data shown, the 4 quads identified in Table 4.2 use the response measured in the next downstream BPM in order to avoid artificial blow-up or suppression of measured  $x_Q$  and  $y_Q$ .

## 4.6 Steering Algorithms

### 4.6.1 Horizontal Steering Algorithm





Horizontal orbit in the ring is controlled by 35 ring dipoles and the pulsed injection magnet (PD), for a ratio of 1 corrector per 2 quads. As the ring dipoles are designed to bend the beam  $10^\circ$ , they are sufficient to correct the background Earth field, which on average bends the beam  $\approx 2.1^\circ$  per cell.

I applied VRUMER simulation to determine an effective algorithm for minimizing first turn orbit position in the quadrupoles by setting the 36 dipoles. As there are 2 quadrupoles per dipole, there are a variety of minimization functions available (aim for the center of either quadrupole, or some weighted combination of the two). I only considered quadrupoles immediately downstream of a given dipole, upstream of the next dipole. In these cases, multiple passes would be necessary to find a "centered" orbit, and relaxation is slow. The 2 downstream quadrupoles are indicated as focusing "F" or defocusing "D" based on polarity in the horizontal plane. The nearest downstream quadrupole for any dipole is focusing (in the standard FODO configuration), as sketched in Fig. 4.3.

I considered steering algorithms with an angle term  $x'$ . In the thin lens approximation for a focusing dipole separated from a defocusing dipole by a drift of distance  $L$ ,  $x'_F \equiv \frac{x_D - x_F}{L}$ . I used  $x'_F \propto x_D - x_F$  to include  $x'_F$  in the RMS minimization term, see Table ??.

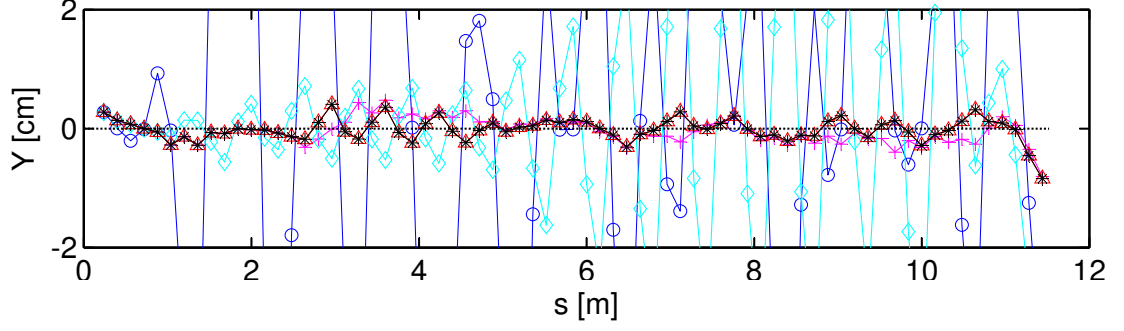
The results of multiple steering algorithms are shown in Table 4.3. Simulated

Tab. 4.3: Different algorithms and their performance (RMS position in quads) for initial condition  $x = 1\text{mm}$ ,  $x' = 0$ .

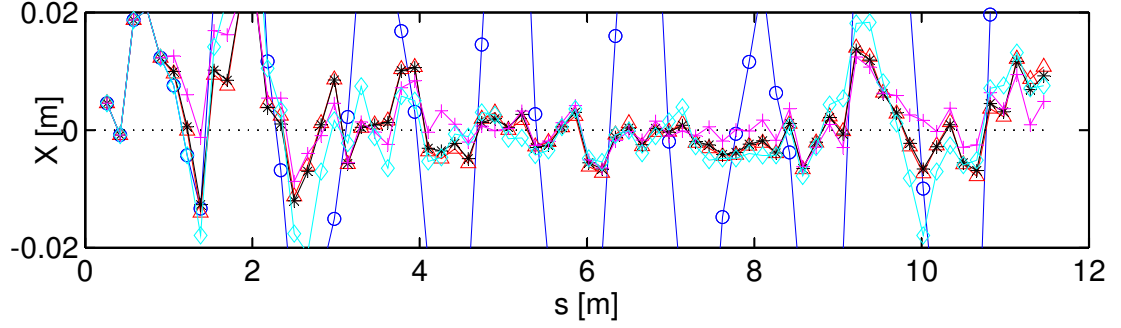
shorthand	Minimization function	RMS( $x_Q$ ) [mm]	RMS( $x_Q$ ) [mm]	plot trace
		no misalign.	$\sigma = 5\text{mm}$	
$x_F$	$\ x_F\ $	5.3	37.3	
$x_D$	$\ x_D\ $	0.2	6.9	
$x_F, x_D$	$\sqrt{x_F^2 + x_D^2}$	2.1	9.3	
$x_F, x'_F$	$\sqrt{x_F^2 + (x_D - x_F)^2}$	0.2	6.6	*
$x_D, x'_F$	$\sqrt{x_D^2 + (x_D - x_F)^2}$	0.2	7.0	

orbits with and without misalignment errors are shown in Fig. 4.7. Qualitatively, the best performers were  $x_D$ ,  $x_F, x'_F$ ,  $x_D, x'_F$ , resulting in almost identical orbits (sub-millimeter differences) that converge very quickly towards the center of the quads given an injection error or quad misalignment.

In the lab, it is much faster to minimize  $x_D$ , as the data collection is faster. It also allows interpolation between scanned dipole settings, as the data can be fit to a line and the zero-crossing calculated (the RMS minimization functions do not lend themselves to fitting by a simple function). However, when applied in the lab, the  $x_F, x'_F$  algorithm seems to yield better results. This may be because of its ability to handle relative misalignments between the focusing and defocusing quadrupoles, as well as reduced sensitivity to nonlinearities in the quad fields and BPM response for large centroid positions. For implementation in the lab (described in Section 4.7), I



(a) No misalignments



(b) Random quad misalignments from Gaussian distribution,  $\sigma = 5\text{mm}$

Fig. 4.7: First turn VRUMER orbits for initial condition  $x = 1\text{mm}$ ,  $x' = 0$ .

chose to use  $x_D$  as the minimization function, due to faster steering time.

#### 4.6.2 Vertical Steering Algorithm

Vertical steering in UMER is accomplished by 18 vertical correction magnets (RSV's) located at the pipe flanges every  $20^\circ$ . All of these magnets are fairly weak (see Table 4.1) and spaced half as densely as horizontal correctors. The largest source of vertical alignment errors is the radial component of the Earth's field, shown in Fig. 4.1. Although the amplitude 200 mG is comparable to the vertical field, the average is only  $< 1\text{ mG}$ .



I use VRUMER to test various vertical steering algorithms and place a lower bound on the best possible first turn orbit using existing vertical steerers, results are shown in Table 4.4. I considered three test cases:

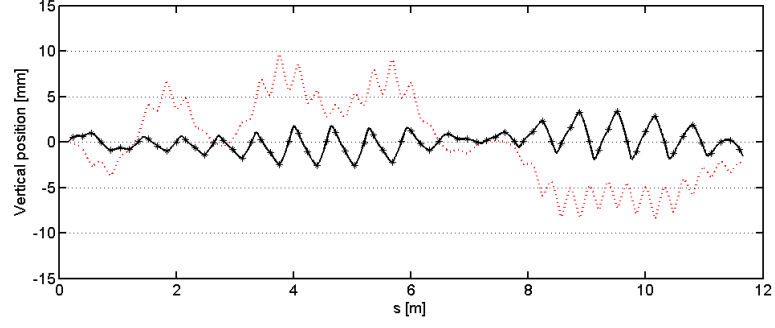
- Ideal: Perfect alignment, RSV current constrained to be  $\leq 10$  A.
- SV limit: Perfect alignment, RSV current limited to  $\leq 2$  A.
- Misaligned: Random misalignment, from Gaussian distribution  $\sigma = 1$  mm, RSV current limited to  $\leq 2$  A.

In summary, in the ideal case (strong correctors, no mechanical misalignments), we can obtain vertical steering with  $\max(y) \sim 3$  mm,  $\text{rms}(y) \sim 1$  mm (Fig. 4.8a). This requires maximum RSV currents in the range 3-4 A, which is not possible given existing heat dissipation limits. If we restrict ourselves to 2 A in the RSVs, the best possible solution is  $\max(y) \sim 7$  mm,  $\text{rms}(y) \sim 2$  mm (Fig. 4.8b). Additionally, allowing for random vertical misalignments of order 1 mm, this increases to  $\max(y) \sim 10$  mm,  $\text{rms}(y) \sim 3 - 4$  mm (Fig. 4.8c).

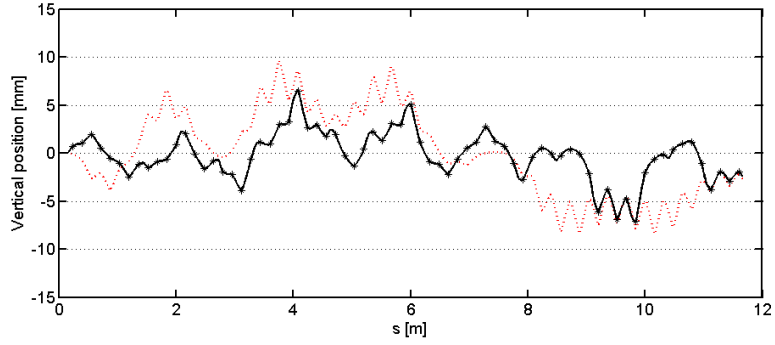
I conclude that the existing vertical correctors provide too weak of a correction to offer significant improvement on the existing first-turn solution. Enhanced vertical correction is necessary to achieve steering comparable to horizontal plane. This is possible through the use of radial field-cancelling Helmholtz coils or through addition of more weak vertical correctors (see Section 4.8).

Tab. 4.4: Vertical steering algorithms and their performance (RMS position in quads)  
for perfect alignment. Subscript indicates quad # counting downstream from  
vertical steerer ( $y_1$  is position in first quad downstream from each RSV).

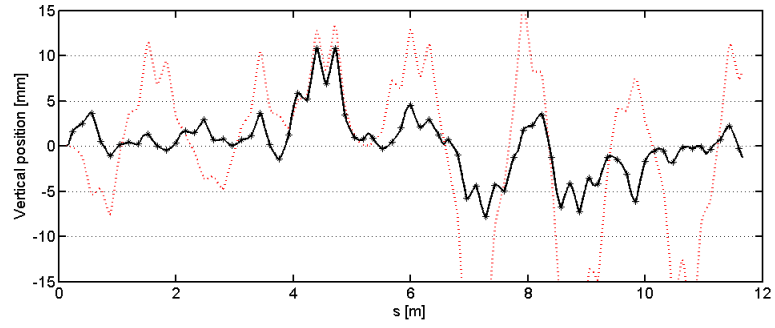
shorthand	Minimization Function	RMS( $y_Q$ ) [mm]	RMS( $y_Q$ ) [mm] SV limit	RMS( $y_Q$ ) [mm] $\sigma = 1\text{mm}$
SV=0	none	4.6	4.6	10.4
$y_1$	$\ y_1\ $	37.0		
$y_3$	$\ y_3\ $	1.5	2.2	3.8
$y_4$	$\ y_4\ $	1.7	2.5	3.4
$y_1, y_2$	$\sqrt{\frac{1}{2}(y_1^2 + y_2^2)}$	25.9		
$y_2, y_3$	$\sqrt{\frac{1}{2}(y_1^2 + y_3^2)}$	1.2	2.5	4.2
$y_3, y_4$	$\sqrt{\frac{1}{2}(y_3^2 + y_4^2)}$	0.98	2.4	3.7
$y_1, y_3$	$\sqrt{\frac{1}{2}(y_1^2 + y_3^2)}$	1.1	2.5	
(focusing)				
$y_2, y_4$	$\sqrt{\frac{1}{2}(y_2^2 + y_4^2)}$	0.93	2.6	4.6
(defocusing)				
$y_1, y'_1$	$\sqrt{\frac{1}{2}(y_1^2 + (y_2 - y_1)^2)}$	18.7		
$y_2, y'_2$	$\sqrt{\frac{1}{2}(y_2^2 + (y_3 - y_2)^2)}$	1.1	2.2	
$y_3, y'_3$	$\sqrt{\frac{1}{2}(y_2^2 + (y_4 - y_3)^2)}$	1.3	2.2	
$y_1, y_2, y_3, y_4$	$\sqrt{\frac{1}{4}(y_1^2 + y_2^2 + y_3^2 + y_4^2)}$	0.95	2.4	5.0



(a) Vertical steering for perfect alignment, no current limit. Steering by minimizing  $\|y_4\|$ . Red dotted trace is vertical solution without steering corrections.



(b) Vertical steering for perfect alignment, RSV current limited to 2 A.



(c) Vertical steering for misalignment of  $\sigma = 1$  mm, RSV current limited to 2 A.

## 4.7 Implementation

This section describes how the quad-as-BPM measurement and quad-centering steering algorithms are applied.

### 4.7.1 Quad-as-BPM position measurement

The process for collecting quadrupole response data and converting to quadrupole position data has been automated and stream-lined into the UMER control system. The procedure is conceptually straightforward. For a specified quadrupole, the algorithm:

1. Grabs a list of functioning BPM's, chooses downstream BPM for measurement of quad response (excluding pairs listed in Table 4.2).
2. Varies quadrupole over a preset range of  $\pm 0.09$  A around nominal set-point, using 5 data points total to calculate response.
3. Calculates response slopes  $\frac{\Delta X_{BPM}}{\Delta I_{quad}}$  and  $\frac{\Delta Y_{BPM}}{\Delta I_{quad}}$  by applying linear least squares fit to response data.
4. Runs VRUMER simulation 9 times to calculate simulated response slope for given quad-BPM pair. Divide  $x_q$ ,  $y_q$  by response slope to determine slope-to-position calibration factor.
5. Applies VRUMER calibration factor to measured response slope to return measured position in quad.

6. Calculates error to response slope, including 95% confidence interval to slope, as well as quad-BPM separation relation to phase advance, according to Eq.

4.6.

Arguably, the slope-to-position calibration factor could be generated using a matrix-based tracking technique (as outlined in [?]) and saved as a look-up table. For a given quad-BPM separation (for 72 quadrupoles there are only 8 possible separations), this number is not expected to change much and this approach would require fewer computations. However, this comes with an added loss of flexibility. The look-up table would have to be recalculated for UMER operating points with different quad focusing strengths or non-FODO orientations. For example, Chapter ?? uses an alternative lattice configuration with half the quads turned off. The time savings for using a look-up table are small. Running VRUMER takes  $\sim 0.06$  seconds, so even for the an entire quad scan (9 points) VRUMER costs  $\sim 0.5$  second per quad. This is negligible compared to the time required to measure BPM response for multiple quad settings.

There is a slight discrepancy with the phase-advance contribution to error bar calculation. The error  $\sigma_\sigma \equiv |\sigma_{exp} - \sigma_{sim}|$ . Simulated phase advance  $\sigma_{sim}$  is estimated from VRUMER results using NAFF algorithm [4], [5]. Experimental phase advance  $\sigma_{exp}$  is hard-coded to be  $\nu_x = 6.636$ ,  $\nu_y = 6.752$  for standard 1.826 A operating point. This will result in erroneously large error bars for different operating points and should be modified in the future to be more general.

#### 4.7.2 *Steering Procedure*

This is a description of the horizontal steering method I used to steer the 6 mA beam on November, 2015. The final solution was saved as settings file `kiersten_6mA_151116.csv`.

The procedure for horizontal steering attempts to steer the beam as close as possible to the center of the quads in the first turn, and use two dipoles at the end of the ring to close the orbit. I generated this solution using an existing solution with many turns, but it should be possible to apply this method to a ring with "no-steering" (significant current loss in the first few turns). The procedure is as follows:

1. Set last 2 injection dipoles by scanning currents and identifying smallest rms deviation in first two RQ's after injection. Time: 1 hour.
2. Steer through RQ3 (first turn) by setting current in D1; Repeat injection scan if change was significant. Time: 10 minutes + 1 hour if repeating injection scan.
3. Steer through quads in first turn, setting dipoles D2-34 in order and using quad-as-BPM method to measure position in quads. Time: 2 1/2 hours ( $\times 2$  for best results).
4. Close orbit by scanning D34 and D35 currents. Time: 30 minutes
5. Verify orbit quality by running quad scan for 1st turn quad-as-BPM data, and look at multi-turn BPM data to estimate orbit excursions from closed orbit.

Time: 30 minutes.

Total (minimum) time for steering:  $\approx 6$  hours. Time estimates are for total measurement/ beam-on time, more time should be added for trouble-shooting and general unruly behavior.

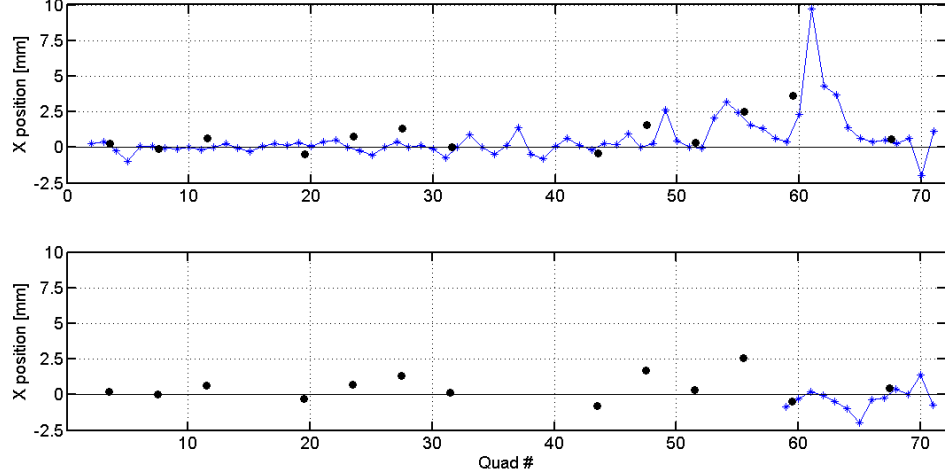


Fig. 4.8: 1st turn solution generated on 11/13/15 (top) and 11/16/15 (bottom), by steering through defocusing quadrupoles.

### *Points Rejection*

A weakness of the  $\|x_D\|$  minimization is that occasionally the data will not fall on a straight line. This is most likely due to scraping between the dipole and BPM or noise in the region near the pulser. In the ring steering scripts, I have implemented a points rejection criteria that throws away quad position data with errorbar  $> 1$  mm. As the errors is proportional to the uncertainty in the fitted slope of the quad response, large non-linearities in the quad response will manifest

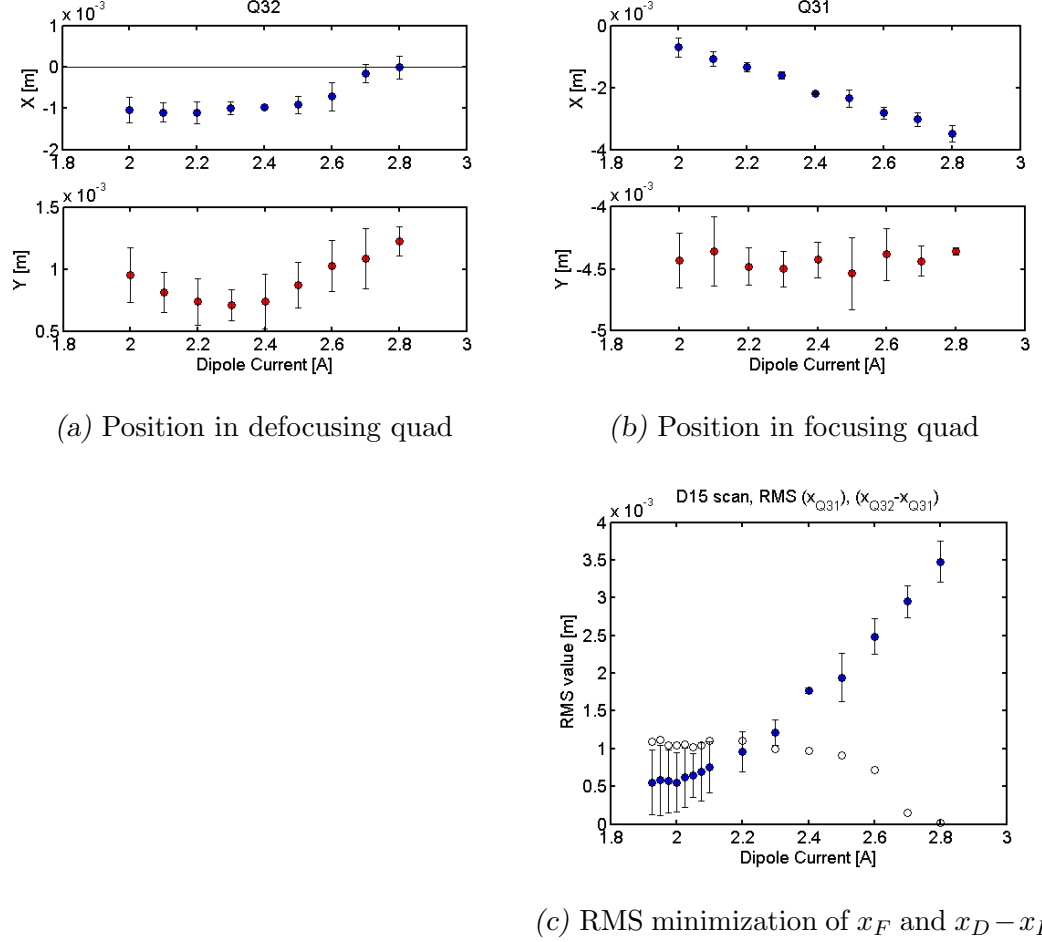


Fig. 4.9: Steering through D15 using two different algorithms, 11/11/15

as large error bars. This is typical of large centroid excursion in either the quad or the BPM.

### *Closing the orbit*

The final step is to set the current in the dipoles near the end of the ring so that the closed orbit is close to the p1 closed orbit. Two dipoles are required for control of  $x$  and  $x'$ . Naively, one would vary the last two dipoles, D35 and PD-Rec. Unfortunately PD-Rec has significant coupling with the first turn beam position.



For a scan of PD-Rec from 8.25  $\rightarrow$  13.75 A, the position of the beam in the first BPM varies in the range  $\Delta x = \pm 2\text{mm}$ . Changing PD-Rec would mean changing all ring dipole settings to compensate, which is undesirable.

It is possible but difficult to optimize the value of PD-Rec. Instead, I assume that the present setting (PD-Rec I= 11 A) is reasonably close to the ideal value such that closing the orbit with D34 and D35 will result in a bump in the closed orbit in that neighborhood. It may be possible to infer, based on the difference in the D34 currents optimized for a) steering through RQ69 and RQ70 and b) a closed orbit solution, the size of the orbit bump.

To set D34 and D35, I scan the currents in each and record the BPM response for the first four turns in the first 3 BPMs. I try to minimize the RMS change in position between turn 1 and turn  $N \leq 4$  in the first three BPM's. For each BPM 1-3, I define an RMS quantity  $\sqrt{\frac{1}{3} [(x_2 - x_1)^2 + (x_3 - x_1)^2 + (x_4 - x_1)^2]}$ . In order to find a good closed orbit, I ran 3 scans, increasing the resolution and/or re-centering the scan range for each successive scan. Scan takes  $\sim 13$  minutes to read 3 BPMs for 11 current settings in each dipole.

### *Corrected Beam Orbit*

## *4.8 Increasing Vertical Steering Capability*

Vertical orbit correction is inherently limited by the strength of vertical corrector magnets, RSV in Table 4.1. Previous assumption has been that sparsely populated, low-field vertical correctors were sufficient to correct for the low average

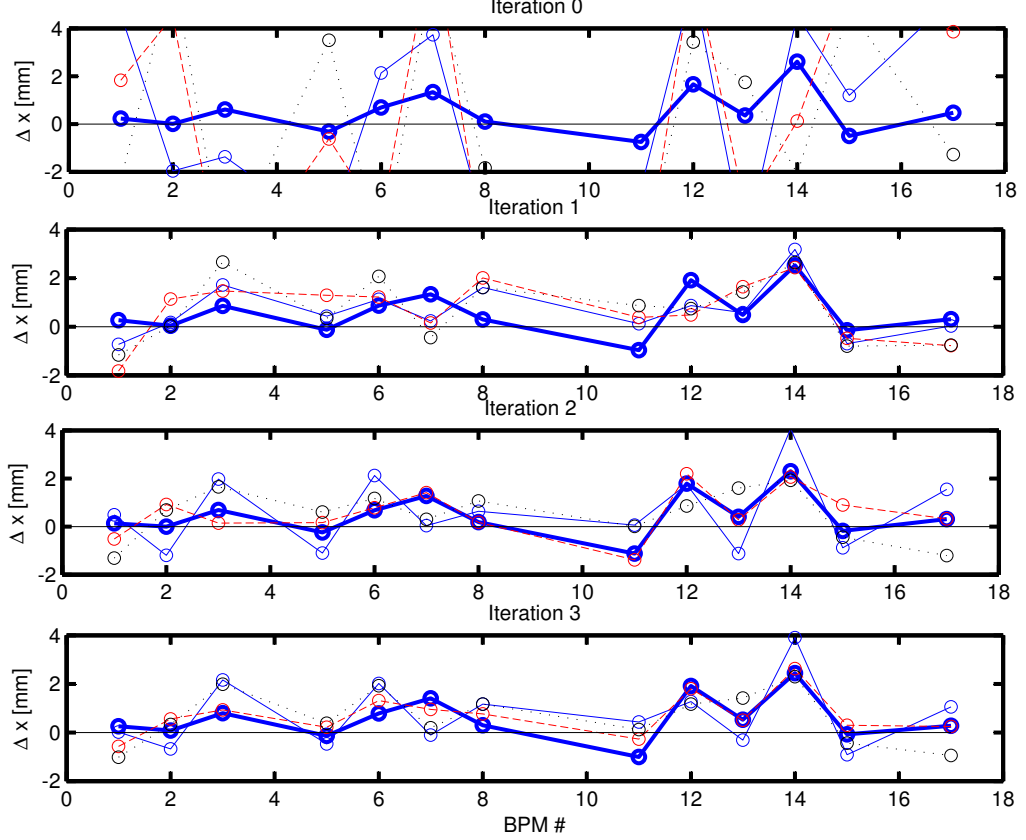


Fig. 4.10: BPM response for first 4 turns, for D34, D35 currents listed in table ?? . 1st turn: heavy blue trace. 2nd turn: solid blue. 3rd turn: long dash red. 4th turn: short dash black.

radial field. However, at regions of locally high radial field, the radial field bends  $\approx 2.1^\circ$  per vertical corrector (every 2 ring cells), while the corrector at maximum safe excitation of 2 A can only supply  $1.2^\circ$  of correction. This results in locally high vertical excursions, as seen in Fig. 4.12a and Fig. 4.12b. In the first turn, the maximum vertical displacement from quad center is 10 mm and the RMS displacement is 3.2 mm.

While good recirculation with small turn-to-turn oscillation amplitude is possible using the existing correctors, alignment of the orbit to the vertical center of the

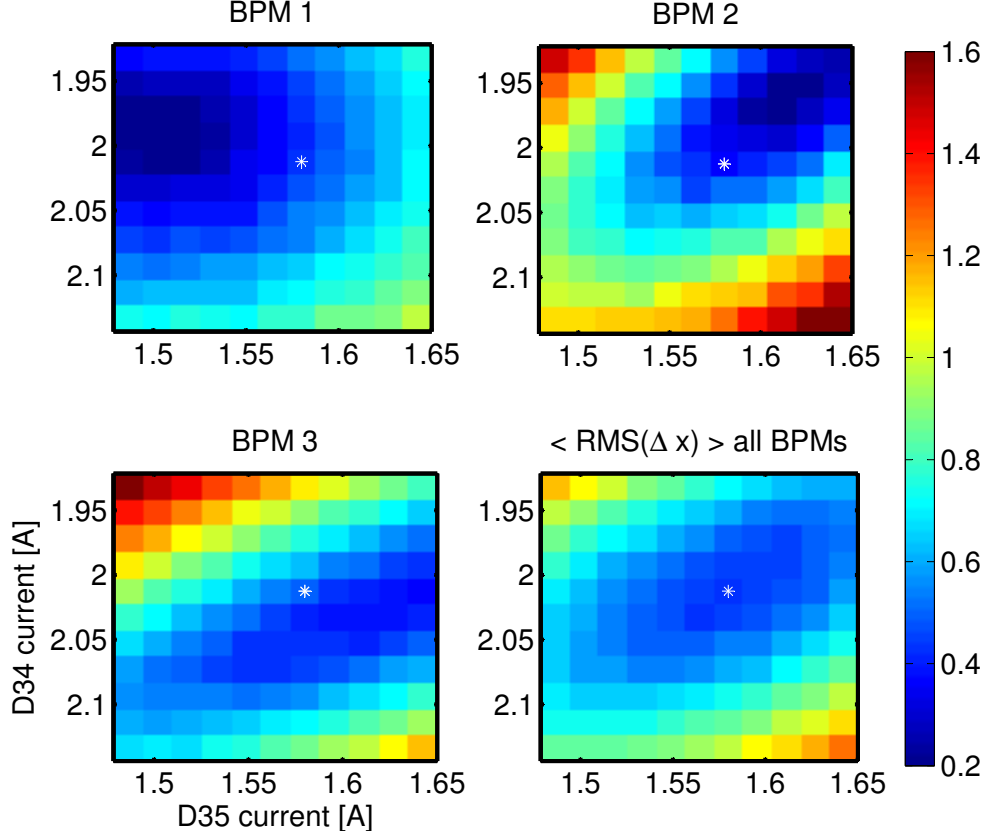
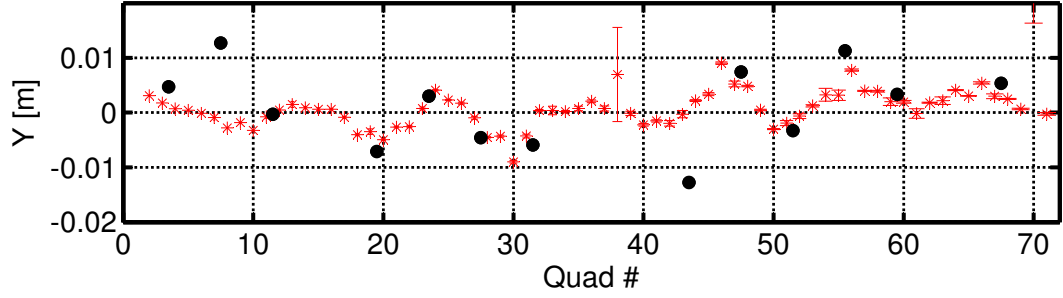


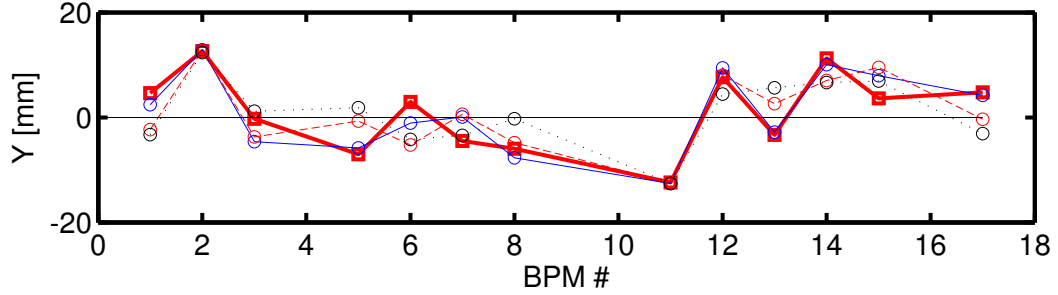
Fig. 4.11: Scan results for first 3 BPMs for iteration 3 in table ???. Color scale is rms value of  $\Delta x$  over first 4 turns [mm], white asterisk indicates optimal setting (D34=2.0129 A, D35=1.5802 A)

quads is limited by the strength and density of vertical correctors. In other words, the beam can be injected with minimum deviation from the closed orbit, but this orbit has large deviations ( $\geq 5$  mm) from the quadrupole centers.

Increased strength and/or density is required for vertical orbit control comparable to horizontal control. I tested the use of "Short Steerers," abbreviated SSV. These are short circuits of length  $\square$  that are used for orbit correction in the injection line, pictured in Fig. ??. There is space in the dense UMER lattice for two additional SSV's per  $20^\circ$  plate, as shown in Fig. 4.12. From Table 4.1, the avail-



(a) Vertical position of 6 mA beam in quads for 1st turn.



(b) Vertical position of 6 mA beam in BPMs for first 4 turns. Note shorted vertical plates at RC2, RC11.

able correction of the SSV is  $\approx 1.2^\circ$  per amp, comparable to RSV strength. With twice the density of the RSV, orbit correction should be sufficient for the  $\approx 2.1^\circ$  of distortion per cell.

The target for steering with the SSV's is second downstream quadrupole, at a distance of  $\approx 12$  cm from the SSV center. Dependence of SSV strength and correction on SSV-target separation is plotted in Fig. 4.13. Similar to dipole steering, choice of "too-close" target leads to over-correction, reflected in the maximum SSV set-point which is at maximum safe current. Longer distances between steerer and target are necessary for corrections within the available strength, and there is a sharp transition between "good steering" and "poor steering" at  $\approx 12$  cm. The

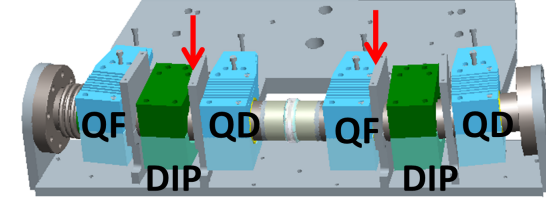


Fig. 4.12: Locations of SSV's on UMER 20° plate indicated with arrows. RSV's are located at vacuum flanges at ends of 20° section.

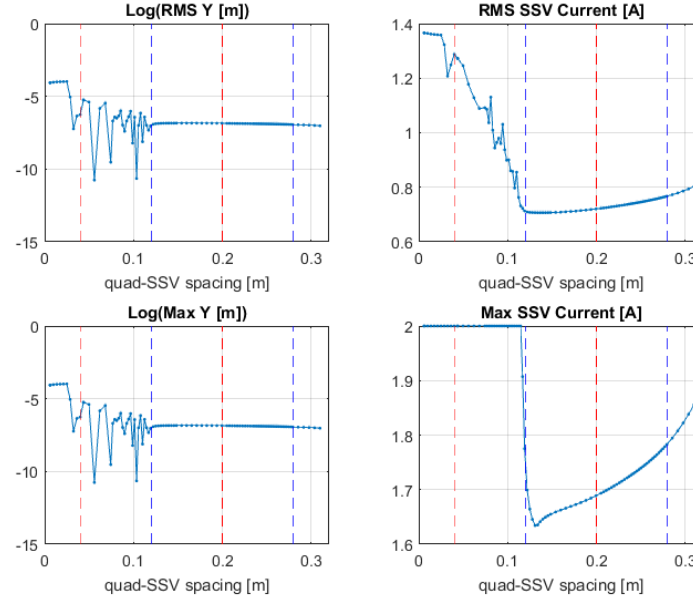


Fig. 4.13: Steering statistics for varying steerer-target distance. Quad center locations are indicated by dashed lines. Red dashes indicate distance from 1st SSV on 20° plate, blue from 2nd SSV on 20° plate.

target quadrupoles for the two SSV locations are at 20 cm and 28 cm respectively, within the range of good correction.

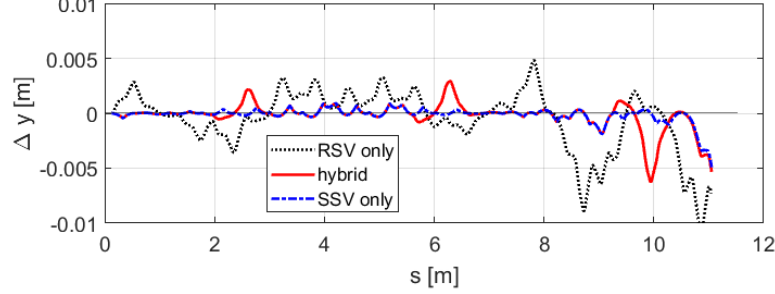
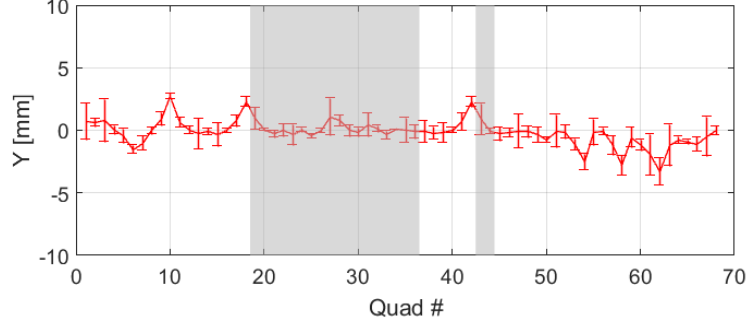


Fig. 4.14: "Best-case" simulated orbits for quad-centered steering with just RSVs, hybrid (SSV's in 28 available locations, plot four RSV's for "glass gap" sections), and 36 SSV's

The resulting first turn orbit with SSV correction from VRUMER calculations is plotted in Fig. 4.14. There are three orbits plotted: orbit correction using only 18 RSV's (black dot), orbit correction using only 36 RSV's (blue dash), and orbit correction using 8 RSV's and 28 SSV's. In the ring, there are 4  $20^\circ$  sections with welded glass gap breaks in the pipe. Extra supports needed to protect the glass inhabit the available SSV space. In these sections, the two RSV's bookending the  $20^\circ$  plate are also utilized. As seen in 4.14, there are large local deviations at the four glass gap sections.

The SSV's were very successful in simulation. To test their effectiveness in the lab, a trial run of 11 SSV's were installed on ring sections 5 - 11 (skipping section 10 due to glass gap in wall current monitor diagnostic). The SSV numbering system corresponds with the nearest horizontal dipole (SSV9 is immediately downstream of



*Fig. 4.15:* Measured first turn orbit for vertical steering with SSV's on 30% of the ring  
(locations indicated by gray shading)

dipole D9, SSV10 upstream of D10, etc). The resulting first turn orbit, using the quad-centering algorithm with RSV1-5, SSV9-18, SSV21-22, RSV10-18 is plotted in Fig. 4.15. Orbit statistics are in Table 4.5. The addition of SSV's reduces the vertical orbit deviation by a factor of  $\approx 2$ , almost to a tolerance of  $\pm 1$  mm.

*Tab. 4.5:* First turn orbit statistics for SSV trial run.

First turn RMS	0.98 mm
First turn Max.	3.25 mm
Shaded RMS	0.45 mm
Shaded Max.	1.11 mm

#### 4.9 *Steering for alternative FODO lattice*

#### 4.10 *Steering for single-channel octupole lattice*

Orbit correction results suggest ring section 9 (location of quadrupole magnets # 34-37) as a likely candidate for the octupole channel, as the vertical orbit control has been demonstrated to be within  $\pm 0.1$  mm measured in the quadrupoles on the first turn with addition of SSV corrector magnets. However, leaving room for SSV correctors in the octupole section limits the length of the octupole channel, which should be as long as possible to maximize tune spread. Without the SSV correctors, orbit deviations are likely to be larger.

SSV's should be avoided in the octupole section, but good orbit control with low deviations is essential for preserving the dynamics aperture of the octupole lattice. Other possibilities for orbit correction over a single  $20^\circ$  section include field cancelling Helmholtz coils or  $\mu$ -metal shielding. These should be implemented in both horizontal and vertical planes. Low vertical background field will necessitate increased cooling capabilities for the two dipoles on this section, as they will have to be run  $> 3$  A to produce  $10^\circ$  of bend.

#### 4.11 *Global Optimization of Closed Orbit*

[\[6\]](#) [\[7\]](#), [\[8\]](#)



## Bibliography

- [1] K PoorRezaei. Measurement of closed orbit reponse matrix for umer. Technical report, University of Maryland, IREAP, Dec 2011.
- [2] K PoorRezaei. Measuring beam centroid position inside quadrupoles. Technical report, University of Maryland, IREAP, March 2012.
- [3] R Kishek. First principles tune calculation for umer. Technical report, University of Maryland, IREAP, May 2010.
- [4] J. Laskar. Frequency map analysis and particle accelerators. *Particle Accelerator Conference, Portland*, 1(2), 2003.
- [5] Kevin Pedro. Frequency Mapping Analysis for Nonlinear Dynamics in Particle Accelerators. pages 1–12, 2012.
- [6] Author S Kirkpatrick, C D Gelatt, and M P Vecchi. Optimization by Simulated Annealing. *Science*, 220(4598):671–680, 2015.
- [7] Xiaobiao Huang, Jeff Corbett, James Safranek, and Juhao Wu. An algorithm for online optimization of accelerators. *Nuclear Instruments and Methods in Physics Research, Section A: Accelerators, Spectrometers, Detectors and Associated Equipment*, 726:77–83, 2013.
- [8] L. Dovlatyan. private communication, 2017.